



OPEN

SUBJECT AREAS:

BATTERIES

SYNTHESIS

Received  
28 February 2014Accepted  
11 April 2014Published  
2 May 2014

Correspondence and requests for materials should be addressed to B.-W.C. (bwcho@kist.re.kr) or K.Y.C. (kychung@kist.re.kr)

\* These authors contributed equally to this work.

† Current address:  
Department of  
Materials Science and  
Engineering,  
Northwestern  
University, 2220  
Campus Drive,  
Evanston, IL 60208,  
USA.

# Mechanochemical Synthesis of $\text{Li}_2\text{MnO}_3$ Shell/ $\text{LiMO}_2$ ( $M = \text{Ni}, \text{Co}, \text{Mn}$ ) Core-Structured Nanocomposites for Lithium-Ion Batteries

Jae-Kyo Noh<sup>1,2\*</sup>, Soo Kim<sup>1\*†</sup>, Haesik Kim<sup>1</sup>, Wonchang Choi<sup>1</sup>, Wonyoung Chang<sup>1</sup>, Dongjin Byun<sup>2</sup>, Byung-Won Cho<sup>1</sup> & Kyung Yoon Chung<sup>1</sup>

<sup>1</sup>Center for Energy Convergence, Korea Institute of Science and Technology (KIST), Hwarangno 14-gil-5, Seongbuk-gu, Seoul 136-197, Republic of Korea, <sup>2</sup>Department of Materials Science and Engineering, Korea University, Anam-dong 5-1, Seongbuk-gu, Seoul 136-701, Republic of Korea.

**Core/shell-like nanostructured  $x\text{Li}_2\text{MnO}_3 \cdot (1-x)\text{LiMO}_2$  ( $M = \text{Ni}, \text{Co}, \text{Mn}$ ) composite cathode materials are successfully synthesized through a simple solid-state reaction using a mechanochemical ball-milling process. The  $\text{LiMO}_2$  core is designed to have a high-content of Ni, which increases the specific capacity. The detrimental surface effects arising from the high Ni-content are countered by the  $\text{Li}_2\text{MnO}_3$  shell, which stabilizes the nanoparticles. The electrochemical performances and thermal stabilities of the synthesized nanocomposites are compared with those of bare  $\text{LiMO}_2$ . In particular, the results of time-resolved X-ray diffraction (TR-XRD) analyses of  $x\text{Li}_2\text{MnO}_3 \cdot (1-x)\text{LiMO}_2$  nanocomposites as well as their differential scanning calorimetry (DSC) profiles demonstrate that the  $\text{Li}_2\text{MnO}_3$  shell is effective in stabilizing the  $\text{LiMO}_2$  core at high temperatures, making the nanocomposites highly suitable from a safety viewpoint.**

As the application of lithium-ion batteries continues to expand to higher energy consumption devices, such as electric vehicles (EVs) and electrical energy storage (EES) systems, the development of higher energy density electrode materials is becoming more essential. For cathodes, materials with higher operating voltage windows and larger specific capacities are being intensively studied<sup>1</sup>. As a part of these developments of advanced cathode materials, the layered transition metal oxide, which can accommodate more than one unit of Li per molecule, has been receiving the most attention in recent years<sup>2–6</sup>.

Many studies have attempted to optimize the  $x\text{Li}_2\text{MnO}_3 \cdot (1-x)\text{LiMO}_2$  composite system because its capacity can reach higher than  $200 \text{ mA h g}^{-1}$ . For these composites, the  $\text{LiMO}_2$  component is primarily responsible for lithium deintercalation and intercalation at voltages lower than  $4.5 \text{ V}$  (vs.  $\text{Li}/\text{Li}^+$ ), and  $\text{Li}_2\text{MnO}_3$  acts as the additional capacity reservoir when charging above  $4.5 \text{ V}$  (vs.  $\text{Li}/\text{Li}^+$ )<sup>2–6</sup>, where the irreversible activation of  $\text{Li}_2\text{MnO}_3$  into  $\text{Li}_2\text{O}$  and  $\text{MnO}_2$  occurs during the first charge cycle<sup>2–8</sup>. Generally, the synthesis of  $x\text{Li}_2\text{MnO}_3 \cdot (1-x)\text{LiMO}_2$  (equivalently  $\text{Li}_{1+x}\text{MO}_2$ ) or  $\text{LiMO}_2$  has been performed via co-precipitation or sol-gel methods<sup>9–13</sup>. However, the mechanical treatment of solids, such as the ball milling method, could offer a rather simple and highly efficient process with lower energy consumption and cost<sup>14</sup>, to prepare these electrode materials.

Recently, West *et al.* prepared the  $\text{Li}_2\text{MnO}_3$  and  $\text{LiMO}_2$  components separately and performed the synthesis using a ball-milling-annealing process<sup>15</sup>. These researchers observed that the synthesized composite material exhibited crystallographic characteristics and electrochemical performances similar to those of layered-layered  $0.5\text{Li}_2\text{MnO}_3 \cdot 0.5\text{LiNi}_{0.33}\text{Co}_{0.33}\text{Mn}_{0.33}\text{O}_2$  materials prepared by the conventional co-precipitation process<sup>15</sup>. This result proved that the  $\text{Li}_2\text{MnO}_3$  and  $\text{LiMO}_2$  components do not need to be connected at the atomic level to achieve anomalously high capacities (*i.e.*, capacities greater than  $200 \text{ mA h g}^{-1}$ ). In our previous studies, we used the mechanochemical process to form alloys among nanoparticles<sup>16–20</sup>. We have also recently demonstrated that  $\text{Li}_2\text{MnO}_3$  and  $\text{LiMO}_2$  can be closely integrated as a nanocomposite in a controlled mole ratio via a mechanochemical process<sup>21,22</sup>. To increase the specific capacity of  $\text{LiMO}_2$  ( $M = \text{Ni}, \text{Co}, \text{Mn}$ ), a good strategy is to increase its Ni content<sup>23–26</sup>. However, the cathode material may experience detrimental effects at the surface because the Ni at the surface of the material can be easily oxidized and destabilize the surface of the electrode, resulting in a poorer cycle life and thermal stability<sup>27–31</sup>.



Sun *et al.* developed a cathode material  $\text{Li}[(\text{Ni}_{0.8}\text{Co}_{0.1}\text{Mn}_{0.1})_{0.8}(\text{Ni}_{0.5}\text{Mn}_{0.5})_{0.2}]\text{O}_2$  with a microscale core-shell structure; the  $\text{LiNi}_{0.8}\text{Co}_{0.1}\text{Mn}_{0.1}\text{O}_2$  core yielded a high capacity, while the  $\text{Li}[\text{Ni}_{0.5}\text{Mn}_{0.5}]\text{O}_2$  shell provided high thermal stability<sup>32</sup>. In addition, the material exhibited improved cycling performance, with a capacity retention of 98%<sup>33</sup>. A similar cathode material with an average composition of  $\text{Li}[\text{Ni}_{0.68}\text{Co}_{0.18}\text{Mn}_{0.18}]\text{O}_2$ , fabricated by controlling the volume ratio of the core and shell components, also exhibited superior performance<sup>34</sup>. The results reported by Sun and co-workers demonstrated that the core-shell structure is suitable for improving the electrochemical performance of microscale cathode materials. Thus, it is reasonable to assume that the core/shell-like structure would also be suitable at the nanoscale. If  $x\text{Li}_2\text{MnO}_3 \cdot (1-x)\text{LiMO}_2$  nanocomposites were fabricated with a core/shell-like structure, not only would the stability of the material be high, but it would also exhibit anomalously high capacities.

In this study, we synthesized nanoscale core/shell-like structured  $x\text{Li}_2\text{MnO}_3 \cdot (1-x)\text{LiMO}_2$  composites for use as cathode materials. The shell was  $\text{Li}_2\text{MnO}_3$ , while the Ni-rich  $\text{LiNi}_{0.5}\text{Co}_{0.2}\text{Mn}_{0.3}\text{O}_2$  component formed the core. The nanocomposites were fabricated via a solid-state reaction using a mechanochemical process. The uniform  $\text{Li}_2\text{MnO}_3$  coating on the outer surface stabilized the Ni-rich  $\text{LiMO}_2$  cores, as illustrated in Figure 1. We tested various mole ratios of the two components,  $\text{Li}_2\text{MnO}_3$  and  $\text{LiMO}_2$ , to optimize the amount of the surface-coating-forming component ( $\text{Li}_2\text{MnO}_3$ ). We also tested various heat treatment temperatures to investigate whether the temperature had any effect on the structures and electrochemical performances of the nanocomposites. Finally, we investigated whether the thermal stabilities of electrodes formed using the nanocomposite materials were more stable than those of electrodes based on  $\text{LiMO}_2$  alone.

## Results

**Morphologies of the synthesized nanocomposites.** Figure 2 presents the bright field (BF) images of the  $0.5\text{Li}_2\text{MnO}_3 \cdot 0.5\text{LiMO}_2$  samples after they had been subjected to heat treatment temperatures at 400, 700, and  $1000^\circ\text{C}$ . Note that the scale bars in Figure 2 differ as the particle size of the sample was increased at higher heat treatment temperatures. The particles shown in Figure 2 are primary particles, separated from the secondary particles to obtain the transmission electron microscopy (TEM) images. Based on the TEM image in Figure 2 (a), it can be surmised that nanoscale  $\text{Li}_2\text{MnO}_3$  formed at  $400^\circ\text{C}$  and completely covered the surface of the  $\text{LiMO}_2$  particles.

Because the particles of the  $\text{Li}_2\text{MnO}_3$  sample synthesized at  $400^\circ\text{C}$  are much smaller ( $<50\text{ nm}$ )<sup>7</sup> than those of the starting material of  $\text{LiMO}_2$  (average secondary particle size of  $\sim 10\ \mu\text{m}$  before the mechanochemical process), we believe that the  $\text{Li}_2\text{MnO}_3$  layer formed on the surfaces of the  $\text{LiMO}_2$  primary particles after the mechanochemical process and the subsequent heat treatment. With an increase in the heat treatment temperature to  $700^\circ\text{C}$ , the particle size of  $\text{Li}_2\text{MnO}_3$  increased, as observed in Figure 2 (b)<sup>7</sup>. The TEM image in Figure 2 (c) also reveals that larger  $\text{Li}_2\text{MnO}_3$  particles existed on the surfaces of the  $\text{LiMO}_2$  particles even after the heat treatment at  $1000^\circ\text{C}$  and that the overall particle size increased with the heat treatment temperature. In addition, scanning electron microscopy (SEM) images of  $x\text{Li}_2\text{MnO}_3 \cdot (1-x)\text{LiNi}_{0.5}\text{Co}_{0.2}\text{Mn}_{0.3}\text{O}_2$ , where  $x$  is 0.3, 0.5, or 0.7, are displayed in Figure S1 (Supplementary Information); the heat treatment temperature was  $700^\circ\text{C}$ . Because of the aggregation of the primary nanoparticles, secondary particles formed after the mechanochemical milling process and the subsequent high-temperature heat treatment; this result was consistent with those of our previous studies<sup>20–22</sup>. To confirm whether the surface coating material was  $\text{Li}_2\text{MnO}_3$  and the bulk material was  $\text{LiNi}_{0.5}\text{Co}_{0.2}\text{Mn}_{0.3}\text{O}_2$ , we employed energy dispersive X-ray spectroscopy (EDS) to investigate the two materials.

The results of the elemental analysis of the  $0.5\text{Li}_2\text{MnO}_3 \cdot 0.5\text{LiMO}_2$  nanocomposite sample prepared at  $1000^\circ\text{C}$  are presented in Figures 3 (b), (c), and (d). The elements Ni, Co, and Mn are present at the centers of the particles of the nanocomposite material (see Figure 3 (b)). However, upon observing the surfaces of the particles, it was observed that the element Mn was present on the surfaces in the greatest amount, while Ni and Co were present in much smaller amounts (see Figures 3 (c) and (d)). We believe that this result occurred because during the high-temperature heat treatment at  $1000^\circ\text{C}$ , the mixing of the metal cations caused the movement of the transition metals between the  $\text{Li}_2\text{MnO}_3$  surface and the  $\text{LiMO}_2$  bulk; however, the shells of the synthesized electrode materials were designed to be Mn-rich to enhance stabilization.

We also performed elemental mapping for the  $0.5\text{Li}_2\text{MnO}_3 \cdot 0.5\text{LiMO}_2$  nanocomposite sample prepared at  $1000^\circ\text{C}$ ; the results are presented in Figs. 3 (e), (f), and (g). The elemental map shows the concentrations of Mn, Co, and Ni. It was evident that Co and Ni were present in smaller amounts at the surface than was Mn. Upon considering the results of the EDS analyses in combination with the elemental concentration maps, it could be surmised that the mechanochemical process was highly effective for synthesizing core/

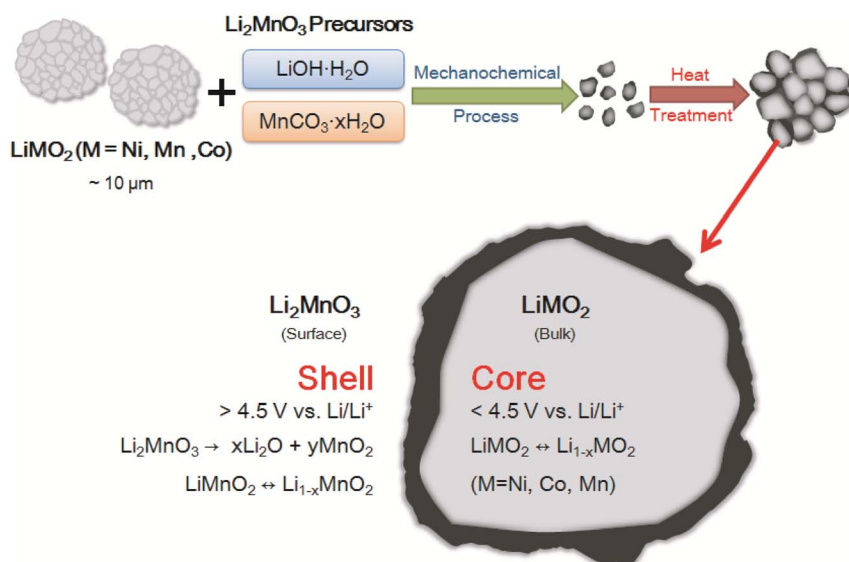


**Figure 1** | Schematic of the core/shell-like nanostructure:  $\text{Li}_2\text{MnO}_3$  surface coating on  $\text{LiMO}_2$  (M = Ni, Co, Mn) bulk electrode materials.

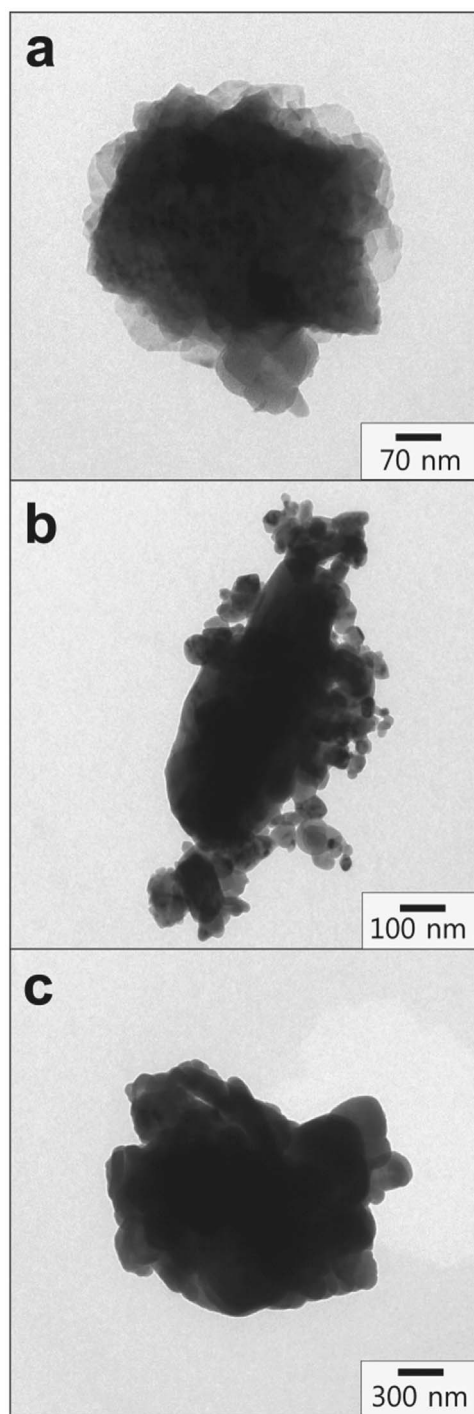


**Figure 2** | BF images of  $0.5\text{Li}_2\text{MnO}_3 \cdot 0.5\text{LiNi}_{0.5}\text{Co}_{0.2}\text{Mn}_{0.3}\text{O}_2$  heat treated at (a)  $400^\circ\text{C}$ , (b)  $700^\circ\text{C}$ , and (c)  $1000^\circ\text{C}$ .

shell-like nanostructures. Furthermore, the nanostructures prepared were such that the  $\text{Li}_2\text{MnO}_3$  played the role of stabilizing the  $\text{LiMO}_2$  core. Finally, to further investigate the crystal structures of  $\text{Li}_2\text{MnO}_3$  and  $\text{LiMO}_2$ , high-resolution (HR) TEM was used to image the  $0.5\text{Li}_2\text{MnO}_3 \cdot 0.5\text{LiMO}_2$  nanocomposite sample prepared at  $1000^\circ\text{C}$ ; the image is presented in Figure S2 (Supplementary Information). The fast Fourier transform (FFT) patterns of the images confirmed the existence of both  $C2/m$   $\text{Li}_2\text{MnO}_3$  and  $R-3m$   $\text{LiMO}_2$ . This result confirmed that the two components closely integrated with each other at their interfacial region.

**Structures of the synthesized nanocomposites.** Figure 4 presents the X-ray diffraction (XRD) profiles of (a)  $\text{Li}_2\text{MnO}_3$ , (b)

$\text{LiNi}_{0.5}\text{Co}_{0.2}\text{Mn}_{0.3}\text{O}_2$ , and the  $0.5\text{Li}_2\text{MnO}_3 \cdot 0.5\text{LiMO}_2$  nanocomposite samples heat treated at (c)  $400^\circ\text{C}$ , (d)  $700^\circ\text{C}$ , and (e)  $1000^\circ\text{C}$ ; the values of  $2\theta$  range from  $15$  to  $70^\circ$ . The XRD patterns of all the nanocomposite samples consisted of overlapping peaks of  $\text{Li}_2\text{MnO}_3$  and  $\text{LiMO}_2$ . All the diffraction peaks could be indexed as being attributable to a hexagonal structure with the space group  $R-3m$ . The image on the right in Figure 4 (a) shows a magnified version of the XRD patterns for  $2\theta$  values ranging from  $20$  to  $24^\circ$ . The low-intensity peaks correspond to the cation ordering in the  $\text{Li}_2\text{MnO}_3$  layer<sup>2-8</sup>. With increases in the heat treatment temperature, the intensities of these peaks also increased. While the  $0.5\text{Li}_2\text{MnO}_3 \cdot 0.5\text{LiMO}_2$  nanocomposite sample heated at  $400^\circ\text{C}$  exhibited a single broad peak at  $21.1^\circ$ , a double peak ranging from  $21.1$  to  $21.4^\circ$  appeared for the sample heated at  $700^\circ\text{C}$ . In addition, slight shifts in the peaks at  $21.1$  and  $21.7^\circ$  were observed for the  $0.5\text{Li}_2\text{MnO}_3 \cdot 0.5\text{LiMO}_2$  sample heated at  $1000^\circ\text{C}$ . The fact that the (018) and (110) peaks appeared separately, at  $64.7$  and  $65.7^\circ$ , respectively, suggested that the cation ordering in the nanocomposites was of a high degree and that the nanocomposites exhibited a well-layer structure<sup>34,35</sup>. Figure 4 (b) presents the XRD patterns of the  $x\text{Li}_2\text{MnO}_3 \cdot (1-x)\text{LiMO}_2$  samples (where  $x$  is 0.3, 0.5, or 0.7) heat-treated at  $1000^\circ\text{C}$ . For these samples, low-intensity peaks also appeared at  $21.1$  and  $21.7^\circ$ . As a greater amount of  $\text{Li}_2\text{MnO}_3$  was incorporated into the nanocomposite, the intensities of the peaks lying between  $20^\circ$  and  $24^\circ$  also increased. The diffraction patterns for the  $x\text{Li}_2\text{MnO}_3 \cdot (1-x)\text{LiMO}_2$  samples heat treated at  $400$  and  $700^\circ\text{C}$  are presented in Figures S3 and S4, respectively.

To obtain additional structural information on the core-shell nanocomposite, we calculated the lattice parameters based on the space group  $R-3m$ , which are summarized in Table S1 (Supplementary Information). When the synthesis temperature was increased, the lattice parameters  $a$  and  $c$  decreased and increased, respectively, which implies that the overall  $c/a$  ratio was increased. This result indicates that the lithium ion can be easily de-/intercalated to the cathode hosts due to the expansion in the  $z$ -direction. In addition, we calculated the crystallite size for each sample using the Williamson-Hall method. At each synthesis temperature, as the amount of  $\text{Li}_2\text{MnO}_3$  was increased, the overall crystallite size of the nanocomposite samples decreased. This result was consistent with our TEM results in Figure 2 and demonstrated that the particle sizes of the  $\text{Li}_2\text{MnO}_3$  on the surface were smaller compared with those of the  $\text{LiMO}_2$  particles. As the synthesis temperature increased, the crystallite size of our sample also increased<sup>7</sup>.

**Electrochemical measurements and thermal stabilities.** Galvanostatic charge and discharge measurements were performed using cells containing  $x\text{Li}_2\text{MnO}_3 \cdot (1-x)\text{LiMO}_2$  as the active material. The 1<sup>st</sup> cycle charge and discharge profiles for the  $x\text{Li}_2\text{MnO}_3 \cdot (1-x)\text{LiMO}_2$  samples (where  $x = 0.3, 0.5, \text{ or } 0.7$ ) heat treated at  $400^\circ\text{C}$  are shown in Figure 5 (a). The cell containing  $0.7\text{Li}_2\text{MnO}_3 \cdot 0.3\text{LiMO}_2$  exhibited a charge capacity of  $269.1 \text{ mA h g}^{-1}$ ; however, this cell also exhibited a large and irreversible capacity loss. The cell containing  $0.3\text{Li}_2\text{MnO}_3 \cdot 0.7\text{LiMO}_2$  initially exhibited a lower charge capacity ( $219.9 \text{ mA h g}^{-1}$ ) and lower irreversible capacity. Figure 5 (b) shows the 1<sup>st</sup> cycle charge and discharge profiles for the  $x\text{Li}_2\text{MnO}_3 \cdot (1-x)\text{LiMO}_2$  samples heat treated at  $700^\circ\text{C}$ . It was observed that the specific capacity decreased as the amount of  $\text{Li}_2\text{MnO}_3$  incorporated was increased. Typically, the discharge capacity of  $\text{Li}_2\text{MnO}_3$  decreases with an increase in the synthesis temperature because of the resultant increase in the particle size and the decrease in the number of stacking faults in the  $\text{Li}_2\text{MnO}_3$  structure<sup>7</sup>.

Figure 5 (c) shows the 1<sup>st</sup> cycle charge and discharge profiles for the  $x\text{Li}_2\text{MnO}_3 \cdot (1-x)\text{LiMO}_2$  samples heat treated at  $1000^\circ\text{C}$ . The discharge capacities of all the samples were higher, and the samples exhibited significantly smaller losses in their irreversible capacities.

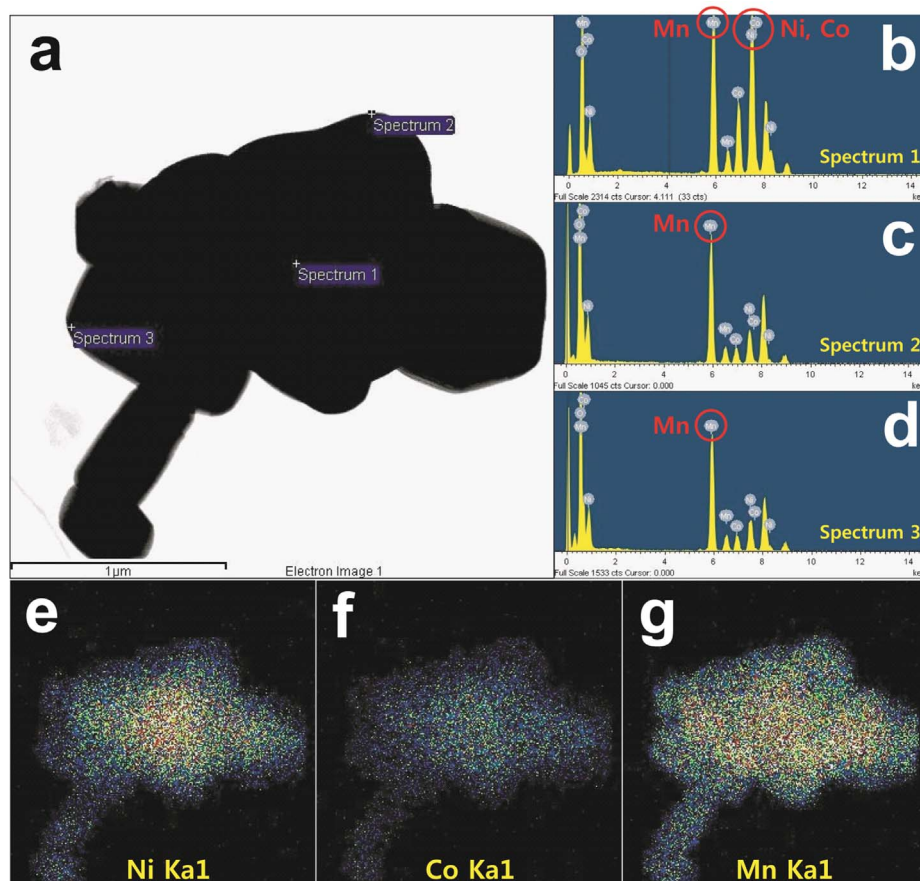


**Figure 3** | EDS point elemental analysis and elemental mapping for  $0.5\text{Li}_2\text{MnO}_3 \cdot 0.5\text{LiNi}_{0.5}\text{Co}_{0.2}\text{Mn}_{0.3}\text{O}_2$  ( $1000^\circ\text{C}$ ). (a) electron image, (b) spectrum 1 (bulk), (c) spectrum 2 (surface), (d) spectrum 3 (surface), and elemental maps for (e) Ni, (f) Co, and (g) Mn.

The cells containing  $0.3\text{Li}_2\text{MnO}_3 \cdot 0.7\text{LiMO}_2$  and  $0.7\text{Li}_2\text{MnO}_3 \cdot 0.3\text{LiMO}_2$  exhibited specific capacities of  $207.2$  and  $206.3 \text{ mA h g}^{-1}$ , respectively. In addition, the discharge capacity of the cell containing  $0.5\text{Li}_2\text{MnO}_3 \cdot 0.5\text{LiMO}_2$  was higher at  $228.9 \text{ mA h g}^{-1}$ . The 1<sup>st</sup> and 2<sup>nd</sup> cycle charge and discharge capacities and efficiencies of the various  $x\text{Li}_2\text{MnO}_3 \cdot (1-x)\text{LiMO}_2$  nanocomposite samples, as well as those of  $\text{Li}_2\text{MnO}_3$  and  $\text{LiNi}_{0.5}\text{Co}_{0.2}\text{Mn}_{0.3}\text{O}_2$ , are listed in Table S2 (Supplementary Information). The nanocomposite cathode materials prepared at  $700$  and  $1000^\circ\text{C}$  exhibited higher 1<sup>st</sup> cycle efficiencies than those of  $\text{Li}_2\text{MnO}_3$  and  $\text{LiMO}_2$ . After  $\text{Li}_2\text{MnO}_3$  activation resulting from charging during the 1<sup>st</sup> cycle, the nanocomposite samples synthesized at  $700$  and  $1000^\circ\text{C}$  exhibited efficiencies greater than 90% during the 2<sup>nd</sup> cycle. The rate capabilities of the coin cells containing the  $x\text{Li}_2\text{MnO}_3 \cdot (1-x)\text{LiMO}_2$  samples heat treated at  $1000^\circ\text{C}$  are plotted in Figure 6 (a); the values correspond to different test current rates. The cell containing  $0.3\text{Li}_2\text{MnO}_3 \cdot 0.7\text{LiMO}_2$  exhibited initial discharge capacities as high as  $207.2$ ,  $188.4$ ,  $171.2$ , and  $147.4 \text{ mA h g}^{-1}$  for test current rates of 10 (1/20 C), 20 (1/10 C), 50 (1/5 C), and 100 (1/2 C)  $\text{mA g}^{-1}$ , respectively. The cell containing  $0.7\text{Li}_2\text{MnO}_3 \cdot 0.3\text{LiMO}_2$  exhibited initial discharge capacities of as high as  $217.5$ ,  $197.1$ ,  $175.8$ , and  $152.6 \text{ mA h g}^{-1}$  at current rates of 10, 20, 50, and 100  $\text{mA g}^{-1}$ , respectively.

Finally, the cell containing  $0.5\text{Li}_2\text{MnO}_3 \cdot 0.5\text{LiMO}_2$  exhibited initial discharge capacities as high as  $237.5$ ,  $219.6$ ,  $198.1$ , and  $174.3 \text{ mA h g}^{-1}$  at the current rates of 10, 20, 50, and 100  $\text{mA g}^{-1}$ , respectively. Thus, when the  $\text{Li}_2\text{MnO}_3/\text{LiMO}_2$  mole ratio was 0.5 : 0.5, the nanocomposite sample heat treated at  $1000^\circ\text{C}$  exhibited specific capacities higher than those of the other materials. The cycling characteristics of the cell based on the  $0.5\text{Li}_2\text{MnO}_3 \cdot 0.5\text{LiMO}_2$  sample heat treated at  $1000^\circ\text{C}$  are shown in Figure 6 (b); the values correspond to 20 cycles,

initial discharge capacities of 2.0 to 4.8 V, and a current rate of  $20 \text{ mA g}^{-1}$  (1/10 C). As mentioned earlier, for the heat treatment temperature of  $1000^\circ\text{C}$ , it was expected that the size of the  $\text{Li}_2\text{MnO}_3$  particles would increase significantly. In the synthesized core/shell-like nanostructures,  $\text{Li}_2\text{MnO}_3$  acts as a coating material. The high-temperature treatment results in the formation of an integrated structure at the interface between the surface layer and the bulk material, which improves the cycling performance. For the sample heat treated at  $1000^\circ\text{C}$ , the  $\text{Li}_2\text{MnO}_3$  outer layer adheres more strongly to the  $\text{LiMO}_2$  bulk material and increases the stability of the nanoparticles. Because the specific capacity of  $\text{Li}_2\text{MnO}_3$  decreases significantly with the temperature<sup>7</sup>, it can be concluded that the role played by the  $\text{Li}_2\text{MnO}_3$  layer in stabilization is of critical importance. In contrast to the results reported by West *et al.*, who prepared  $\text{Li}_2\text{MnO}_3$  and  $\text{LiMO}_2$  separately using ball-milling and subsequent annealing (the processes had to be repeated twice, once for each material), the synthesis technique employed in the current study is simple and robust.

## Discussion

In the synthesized nanocomposites, the  $\text{Li}_2\text{MnO}_3$  component plays a greater role in stabilization because of the core/shell-like structure. The  $\text{Li}_2\text{MnO}_3$  coating, which is present on the outer surfaces of the  $\text{LiMO}_2$  cores, effectively stabilizes the cores comprising the bulk, resulting in improved electrochemical performances. This result is consistent with those of our previous studies<sup>21,22</sup>. In addition to the cost of the synthesis technique employed for fabricating the electrode materials, as well as their initial capacities, rate capabilities, and cyclability, the thermal stability of the materials is another important factor for determining their commercial potential.

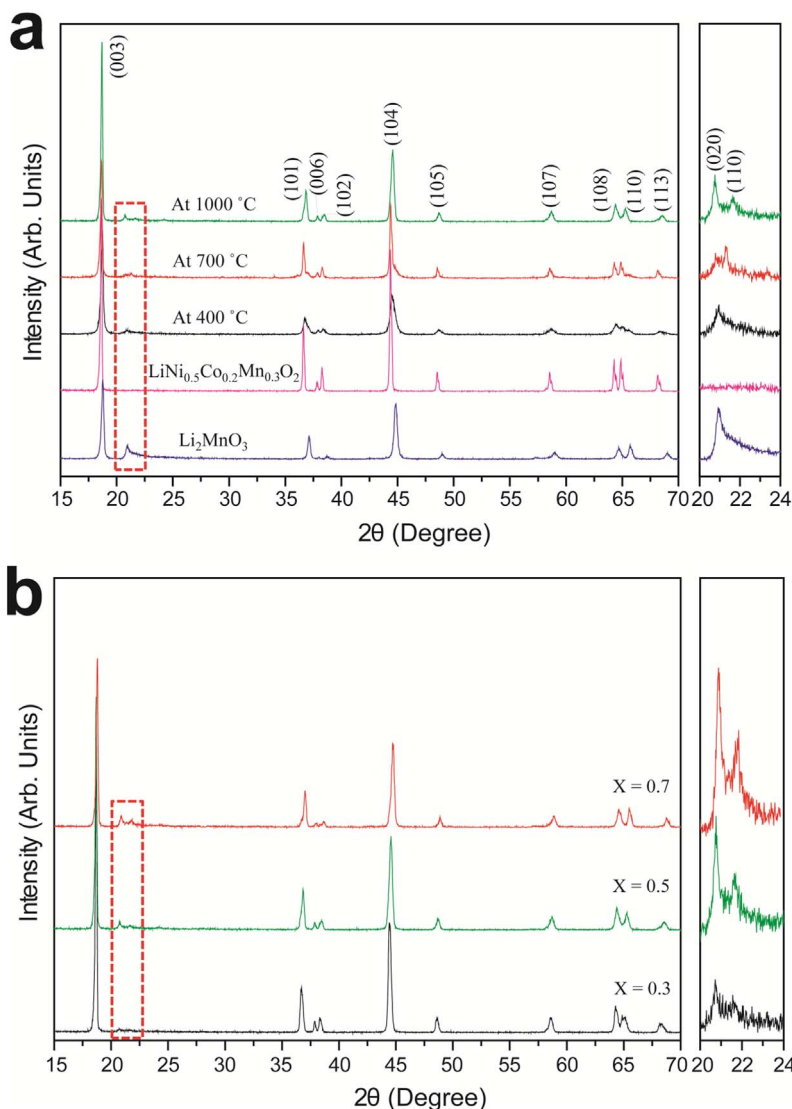


**Figure 4** | X-ray diffraction patterns of (a)  $0.5\text{Li}_2\text{MnO}_3 \cdot 0.5\text{LiNi}_{0.5}\text{Co}_{0.2}\text{Mn}_{0.3}\text{O}_2$  heat treated at 400, 700, and  $1000^\circ\text{C}$  (temperature variation), (b)  $x\text{Li}_2\text{MnO}_3 \cdot (1-x)\text{LiNi}_{0.5}\text{Co}_{0.2}\text{Mn}_{0.3}\text{O}_2$  for  $x = 0.3, 0.5$ , or  $0.7$  and heat treated at  $1000^\circ\text{C}$  (mole ratio variation).

The thermal stabilities of the  $0.5\text{Li}_2\text{MnO}_3 \cdot 0.5\text{LiMO}_2$  and  $\text{LiNi}_{0.5}\text{Co}_{0.2}\text{Mn}_{0.3}\text{O}_2$  nanocomposites after they had been charged to 4.8 V were compared using differential scanning calorimetry (DSC) in a manner similar to that employed by Park *et al.*<sup>36</sup> For  $0.5\text{Li}_2\text{MnO}_3 \cdot 0.5\text{LiMO}_2$ , the sample heat treated at  $1000^\circ\text{C}$  was selected because this sample had exhibited the best electrochemical performance. It can be observed from Figure 7 that the 4.8-V-charged  $\text{LiNi}_{0.5}\text{Co}_{0.2}\text{Mn}_{0.3}\text{O}_2$  sample, whose particles did not have an outer  $\text{Li}_2\text{MnO}_3$  coating, exhibited exothermic peaks corresponding to a two-step dissociation reaction. The temperatures corresponding to the 1<sup>st</sup> and 2<sup>nd</sup> exothermic peaks were 228.68 and  $268.52^\circ\text{C}$ , respectively; this result indicated that the dissociation of the material occurred through a two-step process<sup>36</sup>. The total heat generated during the dissociation reaction was  $461.5 \text{ J g}^{-1}$ . However, only one exothermic peak was observed for the 4.8-V-charged  $0.5\text{Li}_2\text{MnO}_3 \cdot 0.5\text{LiMO}_2$  sample, indicating a one-step dissociation reaction. The peak was positioned at  $248.30^\circ\text{C}$ , and the total heat generated during the reaction was  $239.2 \text{ J g}^{-1}$ , which was lower than that for the bare sample. This result is very similar to those reported by other research groups, who have reported that  $\text{AlF}_3$  or  $\text{FePO}_4$ -coated  $\text{LiMO}_2$  can stabilize the cathode surface and start to decompose only at high temperatures<sup>37,38</sup>. Thus, in addition to exhibiting a higher capacity and improved cyclability (see Figs. 5 and 6), the core/

shell-like structured  $0.5\text{Li}_2\text{MnO}_3 \cdot 0.5\text{LiMO}_2$  sample also exhibited a reduction in the total heat generated and an increase in the dissociation temperature. Therefore, the fact that a greater number of Ni ions were present in the bulk of the electrode resulted in a higher capacity, while the  $\text{Li}_2\text{MnO}_3$  shell improved the overall thermal stability of the  $\text{Li}_2\text{MnO}_3$ -coated materials<sup>37</sup>. The results of the time-resolved (TR) XRD analyses were in good agreement with the DSC results and provided additional information regarding the changes induced in the various nanocomposite samples after heating. Figures 8 (a) and (b) present the TR-XRD patterns of the  $\text{LiNi}_{0.5}\text{Co}_{0.2}\text{Mn}_{0.3}\text{O}_2$  and  $0.5\text{Li}_2\text{MnO}_3 \cdot 0.5\text{LiMO}_2$  samples heat treated at  $1000^\circ\text{C}$  in the absence of an electrolyte; the samples were subsequently heated from room temperature to  $600^\circ\text{C}$  and then charged to 4.8 V. The initial TR-XRD data were collected at  $38^\circ\text{C}$  because the X-ray generator required more than a few minutes to initialize.

We had previously observed that materials with a layered structure undergo phase transformations in the following sequence as the temperature is increased:  $R\text{-}3m \rightarrow Fd3m \rightarrow Fm3m$ . The amount of oxygen released during the phase transformation from  $Fd3m$  to  $Fm3m$  is higher than that generated during the transformation from  $R\text{-}3m$  to  $Fd3m$ <sup>29,30</sup>. Thus, it is important to suppress the phase transformation from  $Fd3m$  to  $Fm3m$  if one wishes to improve the thermal

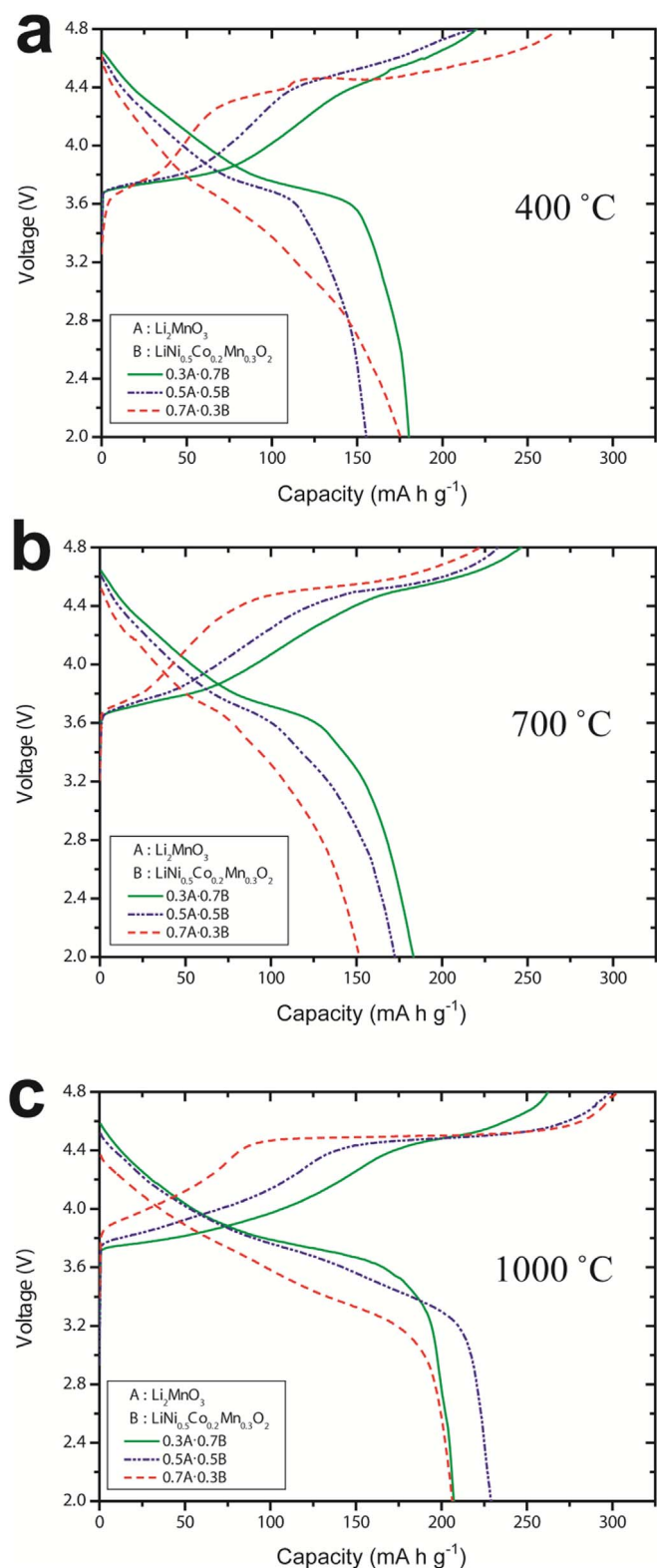


**Figure 5** | 1<sup>st</sup> cycle charge and discharge curves at 10 mA g<sup>-1</sup> (1/20 C) between 2.0 and 4.8 V: (a) 400 °C, (b) 700 °C, and (c) 1000 °C.

stability of such cathode materials. It can be observed from Figure 8 (a) that, at 38 °C, the LiNi<sub>0.5</sub>Co<sub>0.2</sub>Mn<sub>0.3</sub>O<sub>2</sub> sample exhibits a structure belonging to the *R-3m* space group<sup>35,39</sup> (*i.e.*, it has a rhombohedral structure). The change in the structure of the sample commences at approximately 227 °C; this value agrees well with the DSC data, which is presented in Figure 7 (a). Over the temperature range of 200 to

260 °C, which also corresponds to the 1<sup>st</sup> exothermic peak, the (108) and (110) peaks corresponding to the layered structure merged into a (440) peak, which could be indexed to a disordered spinel structure with the space group *Fd3m*<sup>29-31,40</sup>. This result indicated that cation mixing increased over this temperature range<sup>40</sup>. With respect to the 2<sup>nd</sup> exothermic peak (corresponding to a temperature range extending from approximately 240 to 300 °C), the TR-XRD data suggested that the nanocomposite material underwent a phase transformation, with its structure changing from that corresponding to a disordered spinel to that of a rock salt. The (400) and (440) peaks corresponding to the disordered spinel structure disappeared and new (200) and (220) peaks appeared, which could be indexed to the rock salt structure (space group: *Fm3m*). This rock salt structure was preserved at temperatures as high as 600 °C. As observed in Figure 8 (b), the 0.5Li<sub>2</sub>MnO<sub>3</sub>·0.5LiMO<sub>2</sub> sample exhibited a higher thermal stability than that of the LiNi<sub>0.5</sub>Co<sub>0.2</sub>Mn<sub>0.3</sub>O<sub>2</sub> sample.

At 38 °C, the 0.5Li<sub>2</sub>MnO<sub>3</sub>·0.5LiMO<sub>2</sub> sample was observed as having the same structure (*i.e.*, one corresponding to the *R-3m* space group) as the LiNi<sub>0.5</sub>Co<sub>0.2</sub>Mn<sub>0.3</sub>O<sub>2</sub> sample. However, its structure started to change at approximately 244 °C, a temperature much higher than that for the LiNi<sub>0.5</sub>Co<sub>0.2</sub>Mn<sub>0.3</sub>O<sub>2</sub> sample (~227 °C). This value agreed well with the DSC data, which is presented in Figure 7 (b). Further, this temperature is higher than all the previously reported values, which are 223 °C for Li<sub>0.33</sub>Ni<sub>0.5</sub>Co<sub>0.2</sub>Mn<sub>0.3</sub>O<sub>2</sub><sup>40</sup> and 236 °C for Li<sub>0.33</sub>Ni<sub>1/3</sub>Co<sub>1/3</sub>Mn<sub>1/3</sub>O<sub>2</sub><sup>41</sup>. It was evident that the layered structure dissociated based on the gradual decrease in the intensities of the (105), (107), and (113) peaks starting at approximately 244 °C. The appearance of the (311), (400), and (440) peaks confirmed the formation of a new phase starting at 339 °C. The formation of this new phase occurred over the range of 339 to 465 °C and was accompanied by the appearance of peaks corresponding to the LiM<sub>2</sub>O<sub>4</sub>-type spinel structure. Over the temperature range of 339 to 465 °C, in addition to the peaks corresponding to the layered structure, the spinel structure coexisted over this temperature range. These results indicate that the core/shell-like structure of the nanocomposite 0.5Li<sub>2</sub>MnO<sub>3</sub>·0.5LiMO<sub>2</sub> not only retarded the transformation of its structure to the spinel structure at high temperatures but also slowed down its dissociation, increasing its thermal stability. However, in contrast to the observations for LiNi<sub>0.5</sub>Co<sub>0.2</sub>Mn<sub>0.3</sub>O<sub>2</sub>, for 0.5Li<sub>2</sub>MnO<sub>3</sub>·0.5LiMO<sub>2</sub>, another change in structure, that into a Mn<sub>3</sub>O<sub>4</sub>-type spinel structure, was also observed. At approximately 490 °C, peaks attributed to Mn<sub>3</sub>O<sub>4</sub> began to appear (these peaks are marked with an asterisk). It is highly likely that this Mn<sub>3</sub>O<sub>4</sub>-like phase was formed by the dissociation of the Li<sub>2</sub>MnO<sub>3</sub> shells. At the end of the heating stage, that is, at 600 °C, 0.5Li<sub>2</sub>MnO<sub>3</sub>·0.5LiMO<sub>2</sub> exhibited a higher thermal stability than LiNi<sub>0.5</sub>Co<sub>0.2</sub>Mn<sub>0.3</sub>O<sub>2</sub>.

To conclude, we mechanochemically synthesized xLi<sub>2</sub>MnO<sub>3</sub>·(1-x)LiMO<sub>2</sub> cathode materials with a core/shell-like nanostructure using a simple solid-state reaction. The synthesis process employed is an easy, one-step, and low-cost method and results in significant improvements in the electrochemical performance of the LiMO<sub>2</sub> component due to the presence of the stabilizing Li<sub>2</sub>MnO<sub>3</sub> shell-like layer on the surfaces of the LiMO<sub>2</sub> particles. The presence of this Li<sub>2</sub>MnO<sub>3</sub> layer was confirmed using TEM, energy-dispersive spectrometry, and elemental mapping. Furthermore, the presence of Li<sub>2</sub>MnO<sub>3</sub> and LiMO<sub>2</sub> on the surfaces and in the bulk, respectively, was also confirmed based on the FFT patterns of the high-resolution transmission electron microscopy (HRTEM) images of the synthesized samples. Of the various samples synthesized, the 0.5Li<sub>2</sub>MnO<sub>3</sub>·0.5LiNi<sub>0.5</sub>Co<sub>0.2</sub>Mn<sub>0.3</sub>O<sub>2</sub> sample synthesized through a heat treatment at 1000 °C exhibited the highest discharge capacity as well as the highest cyclability. The results of the TR-XRD and DSC analyses showed that the synthesized nanocomposite materials exhibited

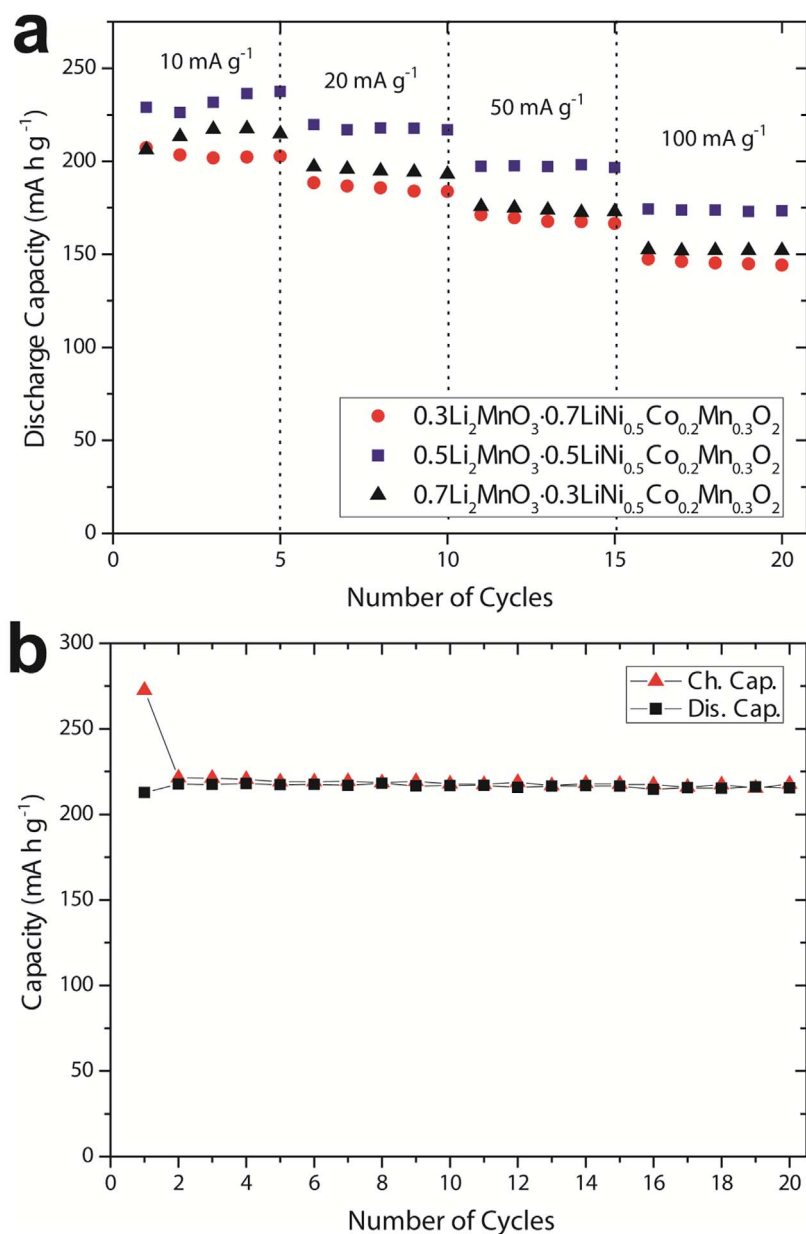


**Figure 6** | (a) Discharge capacities at different C-rates at 1000 °C, (b) cycling performance at 20 mA g<sup>-1</sup> (1/10 C) between 2.0 and 4.8 V of the 0.5Li<sub>2</sub>MnO<sub>3</sub>·0.5LiNi<sub>0.5</sub>Co<sub>0.2</sub>Mn<sub>0.3</sub>O<sub>2</sub> nanocomposite sample heat treated at 1000 °C.

higher thermal stabilities. We propose that the Li<sub>2</sub>MnO<sub>3</sub> coating on the surfaces of the LiMO<sub>2</sub> particles effectively stabilized the electrodes consisting of the Ni-rich bulk material.

## Methods

**Material synthesis.** Stoichiometric amounts of LiOH·H<sub>2</sub>O (≥98%, Aldrich) and MnCO<sub>3</sub>·xH<sub>2</sub>O (≥98%, Aldrich) were used to form the Li<sub>2</sub>MnO<sub>3</sub> shells. The precursors were mixed with LiNi<sub>0.5</sub>Co<sub>0.2</sub>Mn<sub>0.3</sub>O<sub>2</sub> (~10 μm, L&F Materials Co., Ltd., Korea) using a planetary mill (Pulverisette 5, Fritsch) in the presence of acetone at 350 rpm for 3 h; the ball-to-powder weight ratio was 20 : 1<sup>16–22</sup>. Li<sub>2</sub>MnO<sub>3</sub>-stabilized LiMO<sub>2</sub> core/shell-like nanocomposite materials with compositional ratios of 0.3Li<sub>2</sub>MnO<sub>3</sub>·0.7LiMO<sub>2</sub>, 0.5Li<sub>2</sub>MnO<sub>3</sub>·0.5LiMO<sub>2</sub>, and 0.7Li<sub>2</sub>MnO<sub>3</sub>·0.3LiMO<sub>2</sub> were prepared in this study. The heat treatment was performed at 400, 700, or 1000 °C in a box furnace; the heating time was 32 h for the treatment at 400 °C and 10 h for the treatments at 700 and 1000 °C.

**Material characterization.** FESEM (NOVA NanoSEM200, FEI) was used to characterize the morphologies of the prepared materials. Enhanced images were obtained using TEM (CM30, Philips). A TEM system (JEM2100F, JEOL) with an EDS attachment and elemental mapping functionality (Inca Energy, Oxford) was used to investigate the elements present on the surfaces and in the bulk of the synthesized cathode materials. HRTEM (Tecnaï G2, FEI) was used to investigate the crystal

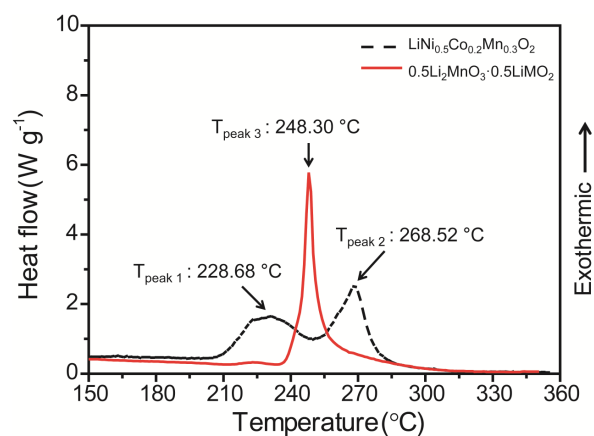


**Figure 7** | DSC profiles for pristine LiNi<sub>0.5</sub>Co<sub>0.2</sub>Mn<sub>0.3</sub>O<sub>2</sub> and the 0.5Li<sub>2</sub>MnO<sub>3</sub>·0.5LiNi<sub>0.5</sub>Co<sub>0.2</sub>Mn<sub>0.3</sub>O<sub>2</sub> sample heat treated at 1000 °C after being charged to 4.8 V vs. Li/Li<sup>+</sup>.

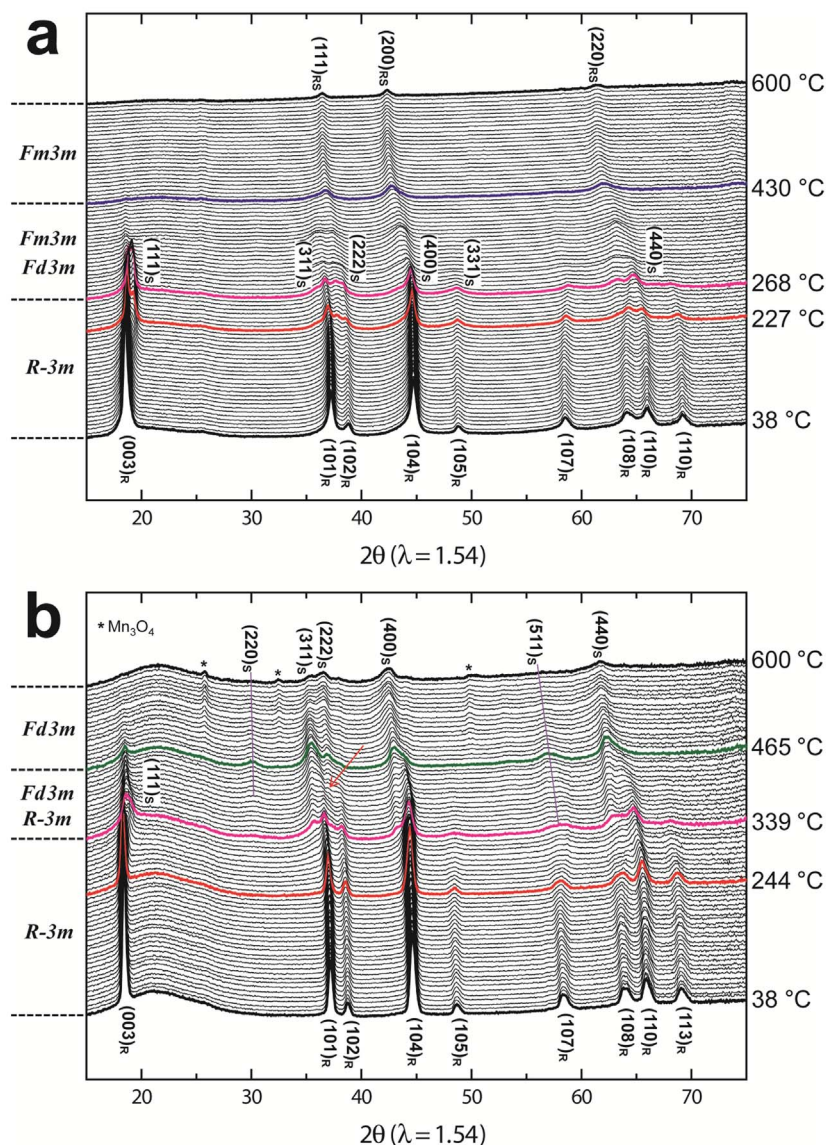


**Figure 8** | TR-XRD patterns of the (a)  $\text{LiNi}_{0.5}\text{Co}_{0.2}\text{Mn}_{0.3}\text{O}_2$  and (b)  $0.5\text{Li}_2\text{MnO}_3 \cdot 0.5\text{LiNi}_{0.5}\text{Co}_{0.2}\text{Mn}_{0.3}\text{O}_2$  samples heat treated at  $1000^\circ\text{C}$  (the temperature was raised to  $600^\circ\text{C}$  after being charged to 4.8 V vs.  $\text{Li}/\text{Li}^+$ ).

structures of the materials based on their FFT patterns. XRD measurements were performed with a Rigaku X-ray diffractometer using monochromatic  $\text{Cu-K}\alpha$  radiation (40 kV and 100 mA). A scan rate of  $3^\circ \text{min}^{-1}$  was selected to collect the diffraction data over  $2\theta$  values ranging from 15 to  $70^\circ$ .

**Electrochemical measurements.** For the electrochemical measurements, coin cells with the CR2032 configuration (Hoshen Corp., Japan) were used. The cells were assembled in a dry room using Li metal for the counter and reference electrodes; Celgard® 2400 was used as the separator. The cathode consisted of a mixture of the synthesized nanocomposite samples, Denka Black®, and polyvinylidene fluoride (PVDF) in 1-methyl-2-pyrrolidone at a weight ratio of 80 : 10 : 10. The electrolyte used was a 1 M solution of  $\text{LiPF}_6$  in an EC : DMC : DEC mixture (1 : 1 : 1 by volume). The cells were stored for 24 h before being subjected to galvanostatic charge-discharge cycling tests. We used a multichannel battery tester (Model 4000, Maccor Inc.) in the constant current/constant voltage (CCCV) mode over potentials ranging from 2.0 to 4.8 V; the test current rate was  $10 \text{ mA g}^{-1}$  (1/20 C) unless noted otherwise.

**Thermal stability analyses.** To determine the thermal stabilities of the charged  $0.5\text{Li}_2\text{MnO}_3 \cdot 0.5\text{LiMO}_2$  ( $1000^\circ\text{C}$ ) electrodes, TR-XRD and DSC analyses were employed. The TR-XRD analyses were performed using an X-ray diffractometry system (R-Axis IV++, Rigaku) at the Korea Institute of Science and Technology (KIST) and at the 1D beamline at Pohang Light Source. Before the analyses, the electrodes were charged fully to 4.8 V. Then, the surfaces of the electrodes were scratched. The obtained powder samples were sealed completely and were mounted on the thermal stage of the TR-XRD system.  $\text{Mo-K}\alpha$  radiation with a wavelength of  $0.7107 \text{ \AA}$  was used for the X-ray diffractometry system at KIST. To allow for a ready comparison of the obtained results with those reported in the

literature, the  $2\theta$  values over which the analyses were performed have been converted into values corresponding to  $\text{Cu-K}\alpha$  radiation ( $\lambda = 1.54 \text{ \AA}$ ). Using the DSC system (Auto Q20, TA Instruments), the thermal stabilities of the electrode materials  $0.5\text{Li}_2\text{MnO}_3 \cdot 0.5\text{LiMO}_2$  ( $1000^\circ\text{C}$ ) and  $\text{LiNi}_{0.5}\text{Co}_{0.2}\text{Mn}_{0.3}\text{O}_2$  were then analyzed, and the capillaries were heated to  $600^\circ\text{C}$  at a heating rate of  $3^\circ\text{C min}^{-1}$ .

1. Tarascon, J.-M. & Armand, M. Issues and challenges facing rechargeable lithium batteries. *Nature*. **414**, 359–367 (2001).
2. Thackeray, M. M. *et al.*  $\text{Li}_2\text{MnO}_3$ -stabilized  $\text{LiMO}_2$  ( $\text{M} = \text{Mn, Ni, Co}$ ) electrodes for lithium-ion batteries. *J. Mater. Chem.* **17**, 3112–3125 (2007).
3. Kang, S. H., Johnson, C. S., Vaughney, J. T., Amine, K. & Thackeray, M. M. The Effects of Acid Treatment on the Electrochemical Properties of  $0.5\text{Li}_2\text{MnO}_3 \cdot 0.5\text{LiNi}_{0.44}\text{Co}_{0.25}\text{Mn}_{0.31}\text{O}_2$  Electrodes in Lithium Cells. *J. Electrochem. Soc.* **153**, A1186–A1192 (2006).
4. Thackeray, M. M., Kang, S. H., Johnson, C. S., Vaughney, J. T. & Hackney, S. A. Comments on the structural complexity of lithium-rich  $\text{Li}_{1+x}\text{M}_{1-x}\text{O}_2$  electrodes ( $\text{M} = \text{Mn, Ni, Co}$ ) for lithium batteries. *Electrochem. Commun.* **8**, 1531–1538 (2006).
5. Johnson, C. S., Li, N., Lefief, C. & Thackeray, M. M. Anomalous capacity and cycling stability of  $x\text{Li}_2\text{MnO}_3 \cdot (1-x)\text{LiMO}_2$  electrodes ( $\text{M} = \text{Mn, Ni, Co}$ ) in lithium batteries at  $50^\circ\text{C}$ . *Electrochem. Commun.* **9**, 787–795 (2007).
6. Kang, S. H. *et al.* Interpreting the structural and electrochemical complexity of  $0.5\text{Li}_2\text{MnO}_3 \cdot 0.5\text{LiMO}_2$  electrodes for lithium batteries ( $\text{M} = \text{Mn}_{0.5-x}\text{Ni}_{0.5-x}\text{Co}_{2x}$ ,  $0 \leq x \leq 0.5$ ). *J. Mater. Chem.* **17**, 2069–2077 (2007).
7. Yu, D. Y. W., Yanagida, K., Kato, Y. & Nakamura, H. Electrochemical Activities in  $\text{Li}_2\text{MnO}_3$ . *J. Electrochem. Soc.* **156**, A417–A424 (2009).



8. Rossouw, M. H., Kock, A., Picciotto, L. A. & Thackeray, M. M. Structural aspects of lithium-manganese-oxide electrodes for rechargeable lithium batteries. *Mat. Res. Bull.* **25**, 173–182 (1990).
9. Gopukumar, S., Chung, K. Y. & Kim, K. B. Novel synthesis of layered  $\text{LiNi}_{1/2}\text{Mn}_{1/2}\text{O}_2$  as cathode material for lithium rechargeable cells. *Electrochim. Acta.* **49**, 803–810 (2004).
10. Yoon, W. S. *et al.* Investigation of the Charge Compensation Mechanism on the Electrochemically Li-Ion Deintercalated  $\text{Li}_{1-x}\text{Co}_{1/3}\text{Ni}_{1/3}\text{Mn}_{1/3}\text{O}_2$  Electrode System by Combination of Soft and Hard X-ray Absorption Spectroscopy. *J. Am. Chem. Soc.* **127**, 17479–17487 (2005).
11. Johnson, C. S., Li, N., Lefief, C., Vaughey, J. T. & Thackeray, M. M. Synthesis, Characterization and Electrochemistry of Lithium Battery Electrodes:  $x\text{Li}_2\text{MnO}_3 \cdot (1-x)\text{LiMn}_{0.333}\text{Ni}_{0.333}\text{Co}_{0.333}\text{O}_2$  ( $0 \leq x \leq 0.7$ ). *Chem. Mater.* **20**, 6095–6106 (2008).
12. Liu, J., Reesha-Jayan, B. & Manthiram, A. Conductive Surface Modification with Aluminum of High Capacity Layered  $\text{Li}[\text{Li}_{0.2}\text{Mn}_{0.54}\text{Ni}_{0.13}\text{Co}_{0.13}]\text{O}_2$  Cathodes. *J. Phys. Chem. C.* **114**, 9528–9533 (2010).
13. Koga, H. *et al.*  $\text{Li}_{1.20}\text{Mn}_{0.54}\text{Co}_{0.13}\text{Ni}_{0.13}\text{O}_2$  with Different Particle Sizes as Attractive Positive Electrode Materials for Lithium-Ion Batteries: Insights into Their Structure. *J. Phys. Chem. C.* **116**, 13497–13506 (2012).
14. Boldyrev, V. V. Mechanochemistry and mechanical activation of solids. *Solid State Ionics.* **63–65**, 537–543 (1993).
15. West, W. C., Soler, J. & Ratnakumar, B. V. Preparation of high quality layered-layered composite  $\text{Li}_2\text{MnO}_3\text{-LiMO}_2$  ( $\text{M} = \text{Ni, Mn, Co}$ ) Li-ion cathodes by a ball milling-annealing process. *J. Power Sources.* **204**, 200–204 (2012).
16. Shin, H. C. *et al.* Rate performance and structural change of Cr-doped  $\text{LiFePO}_4/\text{C}$  during cycling. *Electrochim. Acta.* **53**, 7946–7951 (2008).
17. Kim, Y. U., Cho, B. W. & Sohn, H. J. The Reaction Mechanism of Lithium Insertion in Vanadium Tetrphosphide: A Possible Anode Material in Lithium-Ion Batteries. *J. Electrochem. Soc.* **152**, A1475–A1478 (2005).
18. Woo, S. G. *et al.* Electrochemical Characteristics of Ti-P Composites Prepared by Mechanochemical Synthesis. *J. Electrochem. Soc.* **153**, A1979–A1983 (2006).
19. Oh, S. H., Jeon, S. H., Cho, W. I., Kim, C. S. & Cho, B. W. Synthesis and characterization of the metal-doped high-voltage spinel  $\text{LiNi}_{0.5}\text{Mn}_{1.5}\text{O}_4$  by mechanochemical process. *J. Alloys Compd.* **452**, 389–396 (2008).
20. Kim, S. *et al.* Effects of transition metal doping and surface treatment to improve the electrochemical performance of  $\text{Li}_2\text{MnO}_3$ . *J. Electroceram.* **30**, 159–165 (2013).
21. Kim, S. *et al.* Synthesis of layered-layered  $x\text{Li}_2\text{MnO}_3 \cdot (1-x)\text{LiMO}_2$  ( $\text{M} = \text{Mn, Ni, Co}$ ) nanocomposite electrodes materials by mechanochemical process. *J. Power Sources.* **220**, 422–429 (2012).
22. Kim, S. *et al.* Synthesis of layered-layered  $0.5\text{Li}_2\text{MnO}_3 \cdot 0.5\text{LiCoO}_2$  nanocomposite electrode materials by the mechanochemical process and first principles study. *J. Mater. Chem.* **22**, 25418–25426 (2012).
23. Dahn, J. R., Fuller, E. W., Obrovac, M. & Von Sacken, U. Thermal stability of  $\text{Li}_x\text{CoO}_2$ ,  $\text{Li}_x\text{NiO}_2$  and  $\lambda\text{-MnO}_2$  and consequences for the safety of Li-ion cells. *Solid State Ionics.* **69**, 265–270 (1994).
24. Ohzuku, T., Ueda, A. & Nagayama, M. Electrochemistry and Structural Chemistry of  $\text{LiNiO}_2$  (R3m) for 4 Volt Secondary Lithium Cells. *J. Electrochem. Soc.* **140**, 1862–1870 (1993).
25. Deb, A., Bergmann, U., Cramer, S. P. & Cairns, E. J. In Situ X-Ray Absorption Spectroscopic Study of  $\text{Li}_{1.05}\text{Ni}_{0.35}\text{Co}_{0.25}\text{Mn}_{0.4}\text{O}_2$  Cathode Material Coated with  $\text{LiCoO}_2$ . *J. Electrochem. Soc.* **154**, A534–A541 (2007).
26. Noh, H. J., Youn, S., Yoon, C. S. & Sun, Y. K. Comparison of the structural and electrochemical properties of layered  $\text{Li}[\text{Ni}_x\text{Co}_y\text{Mn}_z]\text{O}_2$  ( $x = 1/3, 0.5, 0.6, 0.7, 0.8$  and  $0.85$ ) cathode material for lithium-ion batteries. *J. Power Sources.* **233**, 121–130 (2013).
27. MacNeil, D. D., Lu, Z., Chen, Z. & Dahn, J. R. A comparison of the electrode/electrolyte reaction at elevated temperatures for various Li-ion battery cathodes. *J. Power Sources.* **108**, 8–14 (2002).
28. Jouanneau, S. *et al.* Synthesis, Characterization, and Electrochemical Behavior of Improved  $\text{Li}[\text{Ni}_x\text{Co}_{1-2x}\text{Mn}_x]\text{O}_2$  ( $0.1 \leq x \leq 0.5$ ). *J. Electrochem. Soc.* **150**, A1637–A1642 (2003).
29. Nam, K. W. *et al.* Cathode Materials: Combining In Situ Synchrotron X-Ray Diffraction and Absorption Techniques with Transmission Electron Microscopy to Study the Origin of Thermal Instability in Overcharged Cathode Materials for Lithium-Ion Batteries. *Adv. Funct. Mater.* **23**, 1046–1046 (2013).
30. Bak, S. M. *et al.* Correlating Structural Changes and Gas Evolution during the Thermal Decomposition of Charged  $\text{Li}_x\text{Ni}_{0.8}\text{Co}_{0.15}\text{Al}_{0.05}\text{O}_2$  Cathode Materials. *Chem. Mater.* **25**, 337–351 (2013).
31. Yoon, W. S., Chung, K. Y., McBreen, J. & Yang, X. Q. A comparative study on structural changes of  $\text{LiCo}_{1/3}\text{Ni}_{1/3}\text{Mn}_{1/3}\text{O}_2$  and  $\text{LiNi}_{0.8}\text{Co}_{0.15}\text{Al}_{0.05}\text{O}_2$  during first charge using in situ XRD. *Electrochem. Commun.* **8**, 1257–1262 (2006).
32. Sun, Y. K., Myung, S. T., Kim, M. H., Prakash, J. & Amine, K. Synthesis and Characterization of  $\text{Li}[(\text{Ni}_{0.8}\text{Co}_{0.1}\text{Mn}_{0.1})_{0.8}(\text{Ni}_{0.5}\text{Mn}_{0.5})_{0.2}]\text{O}_2$  with the Microscale Core-Shell Structure as the Positive Electrode Material for Lithium Batteries. *J. Am. Chem. Soc.* **127**, 13411–13418 (2005).
33. Sun, Y. K., Myung, S. T., Kim, M. H., Park, B. C. & Amine, K. Synthesis of Spherical Nano- to Microscale Core-Shell Particles  $\text{Li}[(\text{Ni}_{0.8}\text{Co}_{0.1}\text{Mn}_{0.1})_{1-x}(\text{Ni}_{0.5}\text{Mn}_{0.5})_x]\text{O}_2$  and Their Applications to Lithium Batteries. *Chem. Mater.* **18**, 5159–5163 (2006).
34. Sun, Y. K., Myung, S. T., Park, B. C., Prakash, J., Belharouak, I. & Amine, K. High-energy cathode material for long-life and safe lithium batteries. *Nat. Mater.* **8**, 320–324 (2009).
35. Wu, K. *et al.* Effect of precursor and synthesis temperature on the structural and electrochemical properties of  $\text{Li}(\text{Ni}_{0.5}\text{Co}_{0.2}\text{Mn}_{0.3})\text{O}_2$ . *Electrochim. Acta.* **75**, 393–398 (2012).
36. Park, M. S. *et al.* On the surface modifications of high-voltage oxide cathodes for lithium-ion batteries: new insight and significant safety improvement. *J. Mater. Chem.* **20**, 7208–7213 (2010).
37. Park, B. C. *et al.* Improvement of structural and electrochemical properties of  $\text{AlF}_3$ -coated  $\text{Li}[\text{Ni}_{1/3}\text{Co}_{1/3}\text{Mn}_{1/3}]\text{O}_2$  cathode materials on high voltage region. *J. Power Sources.* **178**, 826–831 (2008).
38. Liu, X., Li, H., Yoo, E., Ishida, M. & Zhou, H. Fabrication of  $\text{FePO}_4$  layer coated  $\text{LiNi}_{1/3}\text{Co}_{1/3}\text{Mn}_{1/3}\text{O}_2$ : Towards high-performance cathode materials for lithium ion batteries. *Electrochim. Acta.* **83**, 253–258 (2012).
39. Yang, K., Fan, L., Guo, J. & Qu, X. Significant improvement of electrochemical properties of  $\text{AlF}_3$ -coated  $\text{LiNi}_{0.5}\text{Co}_{0.2}\text{Mn}_{0.3}\text{O}_2$  cathode materials. *Electrochim. Acta.* **63**, 363–368 (2012).
40. Cho, Y. H. *et al.* Thermal stability of charged  $\text{LiNi}_{0.5}\text{Co}_{0.2}\text{Mn}_{0.3}\text{O}_2$  cathode for Li-ion batteries investigated by synchrotron based in situ X-ray diffraction. *J. Alloys Compd.* **562**, 219–223 (2013).
41. Nam, K. W., Yoon, W. S. & Ya, X. Q. Structural changes and thermal stability of charged  $\text{LiNi}_{1/3}\text{Co}_{1/3}\text{Mn}_{1/3}\text{O}_2$  cathode material for Li-ion batteries studied by time-resolved XRD. *J. Power Sources.* **189**, 515–518 (2009).

## Acknowledgments

This work was supported by the National Research Foundation of Korea Grant funded by the Korean Government (MEST) (NRF-2011-C1AAA001-0030538). This work was also supported by the KIST Institutional Program (Project No. 2E24663).

## Author contributions

J.K.N., S.K., D.B., B.W.C. and K.Y.C. conceived, planned and designed the experiments. J.K.N. and S.K. synthesized the cathode materials and performed TEM, SEM, DSC and electrochemical tests. H.K. performed XRD analysis. W. Chang and W. Choi contributed to discussion TEM and DSC results. J.K.N., S.K. and K.Y.C. wrote the main manuscript. B.W.C. and K.Y.C. supervised the whole processes. All authors reviewed the manuscript.

## Additional information

Supplementary information accompanies this paper at <http://www.nature.com/scientificreports>

Competing financial interests: The authors declare no competing financial interests.

How to cite this article: Noh, J.-K. *et al.* Mechanochemical Synthesis of  $\text{Li}_2\text{MnO}_3$  Shell/ $\text{LiMO}_2$  ( $\text{M} = \text{Ni, Co, Mn}$ ) Core-Structured Nanocomposites for Lithium-Ion Batteries. *Sci. Rep.* **4**, 4847; DOI:10.1038/srep04847 (2014).



This work is licensed under a Creative Commons Attribution-NonCommercial-NoDerivs 3.0 Unported License. The images in this article are included in the article's Creative Commons license, unless indicated otherwise in the image credit; if the image is not included under the Creative Commons license, users will need to obtain permission from the license holder in order to reproduce the image. To view a copy of this license, visit <http://creativecommons.org/licenses/by-nc-nd/3.0/>